RSC Advances

PAPER

Cite this: *RSC Adv.*, 2022, **12**, 23454

An efficient and stable iodine-doped nickel hydroxide electrocatalyst for water oxidation: synthesis, electrochemical performance, and stability†

Sheraz Yousaf,[a] Sonia Zulfiqar,[b] H. H. Somaily,[cd] Muhammad Farooq Warsi, *[a] Aamir Rasheed,[a] Muhammad Shahid[e] and Iqbal Ahmad *[f]

Received 23rd June 2022
Accepted 24th July 2022

DOI: 10.1039/d2ra03873k

rsc.li/rsc-advances

The design of oxygen evolution reaction (OER) catalysts with higher stability and activity by economical and convenient methods is considered particularly important for the energy conversion technology. Herein, a simple hydrothermal method was adopted for the synthesis of iodine-doped nickel hydroxide nanoparticles and their OER performance was explored. The electrocatalysts were structurally characterized by powder X-ray diffraction analysis (P-XRD), Fourier transform infrared spectroscopy (FTIR), field emission scanning electron microscopy (FESEM), energy dispersive X-ray spectroscopy (EDX), and BET analysis. The electrochemical performance of the electrocatalysts was assessed by cyclic voltammetry, linear sweep voltammetry, and electrochemical impedance spectroscopy. The abundant catalytic active sites, oxygen vacancies, low charge-transfer resistance, and a high pore diameter to pore size ratio of iodine-doped $Ni(OH)_2$ were responsible for its excellent catalytic activity, whereby OER was initiated even at 1.52 V (*vs.* RHE) and a 330 mV overpotential was needed to reach a 40 mV cm^{-2} current density in 1 M KOH solution. The material also exhibited a low Tafel slope (46 mV dec^{-1}), which suggests faster charge-transfer kinetics as compared to its counterparts tested under the same electrochemical environment. It is worth noting that this facile and effective approach suggests a new way for the fabrication of metal hydroxides rich in oxygen vacancies, thus with the potential to boost the electrochemical performance of energy-related systems.

1 Introduction

The overdependence of people on fossil fuels is causing serious environmental problems. Therefore, it is an urgent need to find sustainable and clean energy sources.[1] Among these, hydrogen (H_2), due to its high combustion value and zero percent environmental pollution, is an ideal source of clean renewable energy.[2,3] Mostly, hydrogen is produced at the industrial level by the stream cracking method, which consumes a huge amount of fossil fuels and thus causes environmental pollution.[4] Among all the reported methods, the production of H_2 gas *via* the electrolysis of water is considered the simplest and most practical.[5,6] This approach produces H_2 gas at its maximum purity.[7] The water-splitting techniques include the oxygen evolution reaction (OER) and the hydrogen evolution reaction (HER). However, the OER discourages the water-splitting process owing to its sluggish OER kinetics and high overpotential requirements for accelerating the reaction.[8] Therefore, there is an essential need to design electrocatalysts that can accelerate the kinetics and reduce the required activation energy for the OER, thus improving the proficiency of the water-splitting reaction.[9]

To date, iridium- and ruthenium-based materials are considered the most active electrocatalysts for OER processes.[10] However, the scarcity, higher cost, and instability of these precious metal-based oxides impede their applications in commercial-scale applications. Therefore, it is highly desirable to design a low cost, easily available, stable, and highly active precious-metal-free electrocatalyst for the OER. In this regard, a lot of researchers have developed earth-abundant electrocatalysts, such as transition metal oxides,[11] their hydroxides,[12]

[a]*Institute of Chemistry, The Islamia University of Bahawalpur, Baghdad-ul-Jadeed Campus, Bahawalpur-63100, Pakistan. E-mail: Farooq.warsi@iub.edu.pk*
[b]*Department of Chemistry, School of Sciences & Engineering, The American University in Cairo, New Cairo, 11835, Egypt*
[c]*Research Center for Advanced Materials Science (RCAMS), King Khalid University, P.O. Box 9004, Abha 61413, Saudi Arabia*
[d]*Department of Physics, Faculty of Science, King Khalid University, P.O. Box 9004, Abha, Saudi Arabia*
[e]*Department of Chemistry, College of Science, University of Hafr Al Batin, P.O. Box 1803, Hafr Al Batin, 31991, Saudi Arabia*
[f]*Department of Chemistry, Allama Iqbal Open University, Islamabad, 44000, Pakistan. E-mail: Iqbal.ahmad@aiou.edu.pk*

† Electronic supplementary information (ESI) available. See https://doi.org/10.1039/d2ra03873k

layered double hydroxides[13] and carbon-based nanomaterials.[14] Among these substitutes, transition metal oxides (and hydroxides), owing to their excellent catalytic properties, have been attracting incredible research interest in the last few years.[15]

Particularly, the cobalt-based alternatives have been developed and are considered as excellent electrocatalysts due to their remarkable performance.[16] However, Ni-based electrocatalysts exhibit lower OER performance than those of Co-based electrocatalysts. On the other hand, they are cheaper, possess greater water oxidation potential, and have abundant reserves.[17] Akbari *et al.* studied the OER activity of Ni/NiO material under alkaline conditions using ferrite ions as an impurity.[18] Hand *et al.* synthesized nickel boride hydroxide-based nanoparticles by a chemical method. The material required an overpotential of 340 mV to deliver a 10 mA cm^{-2} current density under alkaline conditions.[19] Similarly, Liu *et al.* developed a sheet-like $Ni(OH)_2$ nanomaterial by a hydrothermal method. The material required 308 mV overpotential to yield 10 mA cm^{-2} current density.[20] Kim *et al.* designed a β-$Ni(OH)_2$ nanoplate-like electrocatalyst for OER applications. The β-$Ni(OH)_2$ prepared under a hydrogen atmosphere and atmospheric air required 340 and 369 mV overpotentials to achieve a 10 mA cm^{-2} current density under alkaline conditions.[21] Therefore, from commercialization point of view, the performance of Ni-based electrocatalysts needs to be significantly improved.

Nickel hydroxide has advantages over other Ni-based electrocatalysts, such as NiO, $NiCoO_x$, and $NiFeO_x$, due to its polymorph structure with several disorders that act as active sites for electrochemical processes. These structural disorders include stacking faults-type crystal defects, variable hydration, and the effective incorporation of foreign ions.[22] β-$Ni(OH)_2$ is its fully hydrated polymorph form and hydrated water molecules are weakly associated with Ni cations and are unable to form hydrogen bonds with lattice hydroxides.[23] This in turn enhances the water reservoir associated with the conducting centers and hence enhances the electrochemical water-splitting process. Moreover, the strong ionic bonds between Ni^{2+}, O^{2-}, and H^+ within each layer result in weak interaction among the adjacent layers. Therefore, it contains several stacked layers and will result in the effective incorporation of foreign species.[24]

Various strategies have been adopted to improve the electrocatalytic activity of materials based on earth-abundant nickel, including doping with metallic or non-metallic ions, creating binary or ternary composites, forming a hybrid with other conducting materials.[25,26] The addition of foreign non-metal heteroatoms or their anions to improve the OER activity of Ni-based catalysts can have a considerable effect. The doping with halogens is another important strategy to boost the electrocatalytic performance of materials. The electron-acceptor nature of halogen atoms is most important in enhancing the conductivity of materials.[27] Rich oxygen vacancies and lattice defects were introduced in β-FeOOH by means of doping with fluorine. The F-doped samples demonstrated a higher electrochemical active surface area (ECSA) and OER activity.[28] Similarly, Hussain *et al.* synthesized 'F'-doped $Ni(OH)_2$ nanoparticles for water-splitting applications. A lower overpotential of 325 mV was required for achieving a current density of 10 mA cm^{-2}.[29] Furthermore, the incorporation of both cationic and anionic species was possible at lattice points or within the interlayer region. However, the anionic species were located at the lattice hydroxide sites or in between the interlayer region.[22]

Among all the halogen atoms, iodine is the most popular as its doping causes fundamental changes in the molecular orientation and stacking, which can change the electrochemical properties of a material.[30] Moreover, the larger size of iodine causes an increase in the intercalation region, which increases the water reserves among them and increases the ionic mobility. Iodine-doped TiO_2 was fabricated by Li and collaborators following a hydrothermal method. The material was tested for visible-light photocatalysis, and a relative increase in degradation efficiency was observed, which was attributed to the formation of oxygen vacancies by multivalent iodine in the material.[31] Similarly, iodine-doped Bi_2WO_6 nanoplates were also synthesized by Zhang *et al.* following a hydrothermal approach. The material was also tested for the photocatalytic degradation of pollutants. A noticeable improvement in degradation efficiency was observed as a result of the formation of oxygen vacancies and defects in the crystal lattice due to the presence of both I^0 and I^- species.[32] Furthermore, non-metal (N, B, and I)-doped TiO_2 nanotubes were also synthesized following an anodization method. The doped samples demonstrated better efficiency, whereupon the order of the observed efficiency was B:TiO_2 > I:TiO_2 > N:TiO_2 > pure TiO_2. The significant increase in efficiency was attributed to the formation of lattice defects, and changes in the orientation of the electronic cloud and oxygen vacancies. Additionally, the designed materials were not only suggested as suitable for water splitting but also applicable for supercapacitor applications.[33]

Here, we report the synthesis and characterization of an iodine-doped $Ni(OH)_2$-based electrocatalyst for OER. The synthesized I-doped nickel hydroxide electrocatalyst required an overpotential of 330 mV for OER to attain a 40 mA cm^{-2} current density using 1 M KOH solution, which showed it could outperform its counterparts under identical electrochemical tests. The results demonstrate that the efficiency of the catalyst was significantly superior and offers prospects in the fabrication of non-metal-doped materials as an effective electrocatalyst for energy-related applications.

2 Results and discussion

2.1 Structural analysis

The crystalline nature assessment and structural phase analysis of the synthesized electrocatalysts were analyzed by X-ray diffraction analysis. The XRD patterns of the pure $Ni(OH)_2$, I-doped $Ni(OH)_2$, and I_2-loaded $Ni(OH)_2$ are presented in Fig. 1(a). The diffraction pattern of pure nickel hydroxides showed the diffraction peaks at 2θ values of 19.08°, 32.80°, 38.28°, 51.93°, 58.71°, 62.39°, 69.24°, 70.11°, 72.44° corresponding to (001), (199), (101), (102), (110), (111), (200), (103), and (201) planes, respectively. The diffraction profile was characteristic of the pure hexagonal phase of $Ni(OH)_2$ and was in agreement with the JCPD number 01-074-2075. Moreover, the

formation of new crystalline orientations in the case of both I-doped $Ni(OH)_2$ and I_2-loaded $Ni(OH)_2$ were not observed. However, Fig. 1(b) shows the shift of the diffraction peak index for (001) toward lower 2θ values with the increase in peak broadening in the case of I-doped $Ni(OH)_2$ and I_2-loaded $Ni(OH)_2$ compared to their pristine nickel hydroxide. This suggested the successful doping of iodine anions in $Ni(OH)_2$.[34,35] Furthermore, the unit cell parameters of $Ni(OH)_2$, I-doped $Ni(OH)_2$, and I_2-loaded $Ni(OH)_2$ electrocatalysts were calculated using unit cell software and the results are presented in Table 1. Increases in both the unit cell constants and volume were observed, suggesting the doping of iodine in the $Ni(OH)_2$ crystal lattice.[36] The crystallite size was also calculated by the modified Scherrer equation and the results are presented in Table 1. A graph was plotted between $\ln\left(\frac{1}{\cos\theta}\right)$ *vs.* $\ln\beta$ and is shown in Fig. S1.† The crystallite sizes of $Ni(OH)_2$, I-doped $Ni(OH)_2$, and I_2-loaded $Ni(OH)_2$ were 28, 22, and 26 nm, respectively. A decrease in the crystalline size upon the addition of iodine components to the matrix was observed. This decrease in crystallite size was due to the inhibition of the crystallite growth upon the addition of iodine. The crystallite growth was suppressed due to the increment in the energy barrier for the mutual diffusion of grains with a distinct size and orientation caused by the adsorbed iodine species in the presence of KI. Therefore, it could be concluded that the iodine ions were doped in the $Ni(OH)_2$ and occupied the apical sites or surface defect sites of the material.[37,38]

Surface functional groups analysis was carried out by FTIR spectroscopy. The FTIR spectra of nickel hydroxide, I-doped nickel hydroxide, and I_2 loaded nickel electrocatalysts are displayed in Fig. 2. The sharp band around 3635 cm^{-1} corresponded to O–H stretching vibrations of the non-hydrogen bonded hydroxyl group in all the prepared samples.[39] The sharp *iR* band around 498 cm^{-1} corresponded to Ni–O–Ni bending vibrations, whereas the band around 430 cm^{-1} was considered due to Ni–O stretching vibrations.[40] No extra absorption band was observed in the iodine-doped and -loaded $Ni(OH)_2$ electrocatalysts. However, the relative shift of the bands corresponded to a wider range of interactions among the functional groups and these are presented in Table S1.† The narrowing and broadening of absorption bands in the I-doped $Ni(OH)_2$ and I_2-loaded $Ni(OH)_2$ electrocatalysts was attributed to the incorporation of a dopant to the apical or surface defect sites of the material.[41]

As the electrocatalytic activity of the materials was linked to their surface morphology, FESEM analysis was performed to analyze the surface morphology. The FESEM images of the nickel hydroxide, I-doped nickel hydroxide, and I_2-loaded hydroxide electrocatalysts are presented in Fig. 3. It was found that $Ni(OH)_2$ was a bouquet-like material composed of circular and spherical units distributed randomly. However, the random distribution of these units for both I-doped $Ni(OH)_2$ and I_2-loaded $Ni(OH)_2$ electrocatalysts was comparably higher with apparently smaller size. Consequently, the distribution in the case of the doped and loaded samples was increased because of the increase in the energy barrier for the mutual diffusion of

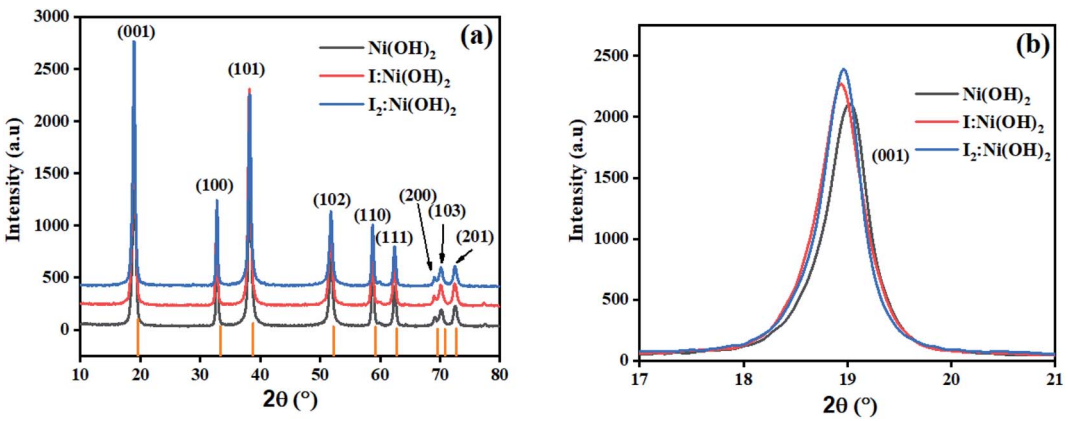

Fig. 1 (a) XRD patterns of $Ni(OH)_2$, I-doped $Ni(OH)_2$, and I_2-loaded $Ni(OH)_2$ electrocatalysts, and (b) the (001) peak shift and broadening in I-doped $Ni(OH)_2$ and I_2-loaded $Ni(OH)_2$ electrocatalysts.

Table 1 XRD parameters of $Ni(OH)_2$, I-doped $Ni(OH)_2$, and I_2-loaded $Ni(OH)_2$ electrocatalysts

S. no.	Material	Crystal system	Cell constants (Å)		Volume $(Å)^3$	Crystallite size (nm)
			a	*c*		
1	$Ni(OH)_2$	Hexagonal	3.13	4.62	39.42	28
2	$I:Ni(OH)_2$	Hexagonal	3.14	4.63	39.64	22
3	$I_2:Ni(OH)_2$	Hexagonal	3.14	4.62	39.49	26

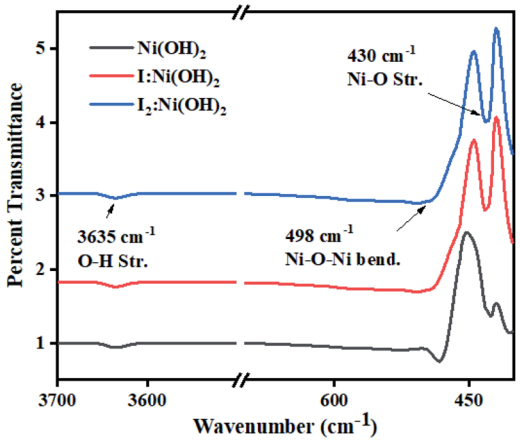

Fig. 2 FTIR spectra of $Ni(OH)_2$, I-doped $Ni(OH)_2$, and I_2-loaded $Ni(OH)_2$ electrocatalysts.

grains induced by the adsorbed iodine species in the presence of KI. This apparent morphology with random distribution of units was responsible for the larger interconnected porous cavities. These porous cavities were then responsible for electrolyte reservoirs, which in turn resulted in the enhanced electrocatalytic activity.[5]

The electrochemical performance for the OER is also related to a material's surface area. Here, adsorption–desorption studies were performed using N_2 gas as an adsorbate on the surface of the catalysts. The resultant BET isotherm is presented in the inset of Fig. S2,† which shows a type IV isotherm with an H3 form of hysteresis loops, indicating the microporous and mesoporous characteristics of the material. The experimental calculated BET surface areas of the $Ni(OH)_2$, I-doped $Ni(OH)_2$, and I_2-loaded $Ni(OH)_2$ electrocatalysts were 36.0, 35.86, and 28.96 $m^2\ g^{-1}$. This decrease in surface area was again due to the increase in the energy barrier as a result of the iodine species. Fig. S2† shows bar-graphs of the pore diameter and area. It was found that with the increase in pore diameter, the pore area also increased. However, the increase in pore area as a function of pore diameter was greater for I-doped $Ni(OH)_2$, which thus had greater porous cavities, thus providing a greater reservoir for electrolyte species, thus resulting in an increase in the OER activity.

The elemental composition of all the prepared electrocatalysts was also examined by EDX spectroscopy and the results are given in Table 2. Fig. 4 shows the EDX spectra of the $Ni(OH)_2$, I-doped $Ni(OH)_2$, and I_2-loaded $Ni(OH)_2$ electrocatalysts. The EDX measurements confirmed the existence of both Ni and O elements in all the synthesized electrocatalysts. However, the presence of iodine could also be recognized in the EDX measurements of the I-doped $Ni(OH)_2$ and I_2-loaded $Ni(OH)_2$ electrocatalysts.[34]

2.2 Preliminary electrochemical investigations

The initial electrochemical characterizations were performed before testing the OER activity of the electrocatalysts. For this,

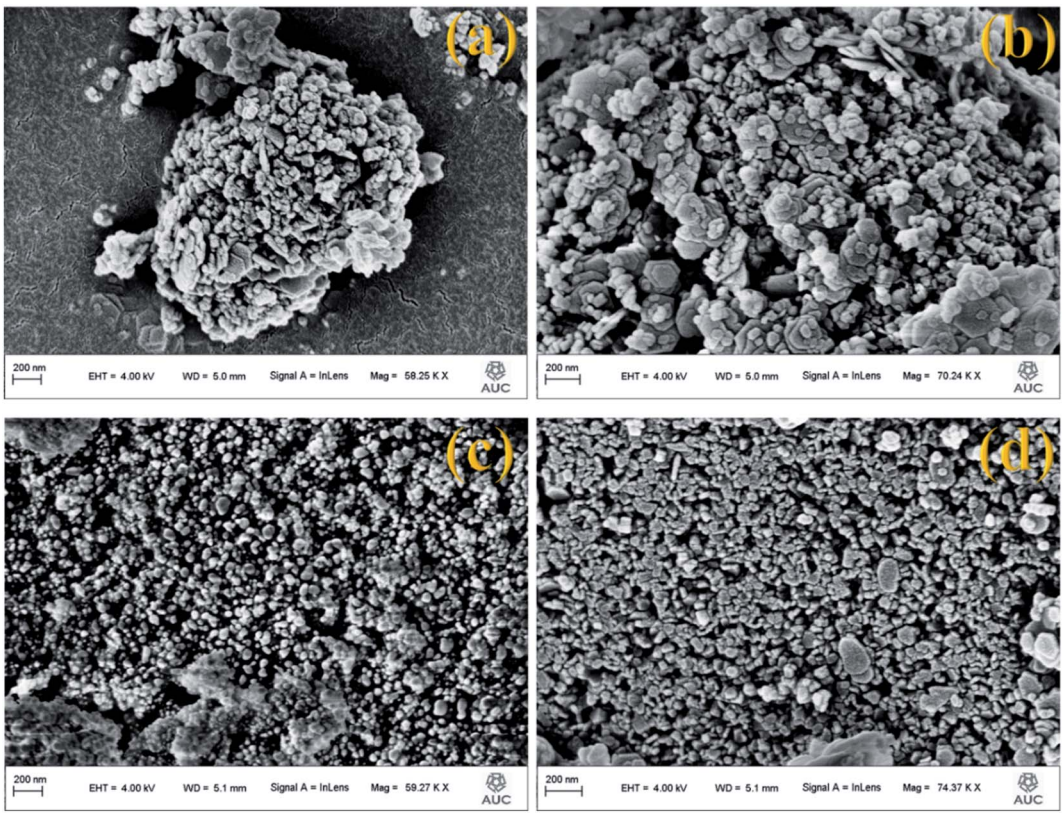

Fig. 3 FESEM images of (a and b) pure $Ni(OH)_2$, (c) I-doped $Ni(OH)_2$, and (d) I_2-loaded $Ni(OH)_2$ electrocatalysts.

Table 2 Elemental composition of the synthesized materials observed from the EDX analysis

S. no.	Sample	Nickel	Oxygen	Iodine
1	$Ni(OH)_2$	59.57	40.43	—
2	I-doped $Ni(OH)_2$	75.42	24.54	0.04
3	I_2-loaded $Ni(OH)_2$	61.65	35.06	3.93

the accessibility of the potential active sites, the active surface area of the electrocatalysts, and their stability before the OER performance evaluation were considered following standard electrochemical methods.[42,43] Cyclic voltammetry (CV) measurements were performed and the results are shown in Fig. S3.† The CV measurements of the bare carbon fiber cloth (CFC) exhibited no redox reactions. However, broad redox peaks were prominent in the case of $Ni(OH)_2$, I-doped $Ni(OH)_2$, and I_2-loaded $Ni(OH)_2$ electrocatalysts. These apparent redox peaks were due to Ni^{2+}/Ni^{3+} formation, which was responsible for the promising electrochemical activity.[44] The electrocatalyst's aging, stability, and activity were investigated by means of measuring consecutive 200 CV cycles at a 100 mV s^{-1} scan rate. It was noted that the shape of the voltammogram changed slightly from the first cycle to the 200th one. However, the current density remained unaffected and did not change drastically. No more extra peaks appeared during the concurrent 200 cycles. These results revealed that the electrodes had attained their highest stability and could be subjected to OER analysis.

Furthermore, the loss in catalytically active sites and their degradation were tested by finding the charge (q^*) associated with these different cycles. Fig. 5(a) shows that the charge under the CV loop remained almost constant with the increase in the

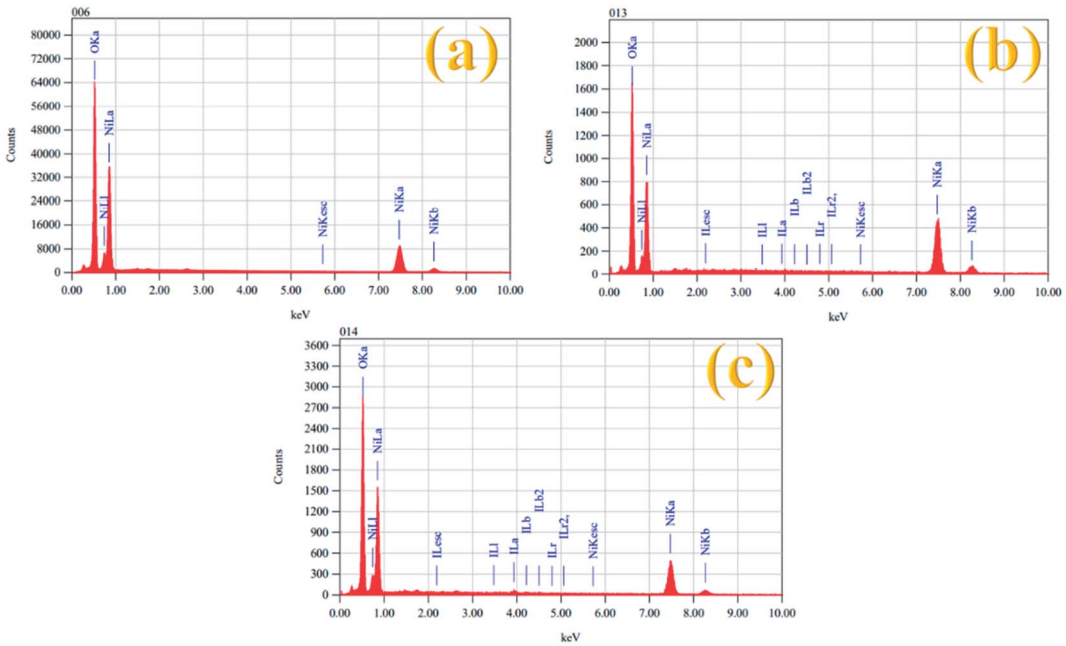

Fig. 4 EDX spectra of (a) $Ni(OH)_2$, (b) I-doped $Ni(OH)_2$, and (c) I_2-loaded $Ni(OH)_2$ electrocatalysts.

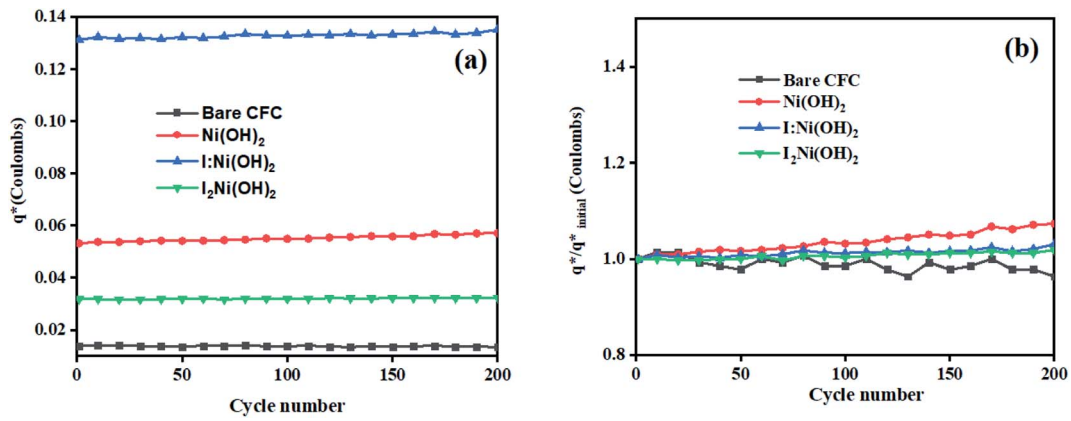

Fig. 5 Electrochemical characterization: (a) charge (q^*) evaluation and (b) $q^*/q^*_{initial}$ fractions throughout the stability tests.

number of cycles. This constant charge under the CV loop suggests that the catalytic behavior of the electrocatalyst was stable and consistent. Fig. 5(b) shows the plot for q^*/q^*_{initial} *vs.* cycle number. As the charges have a direct relation with the electroactive sites, accordingly, the fraction q^*/q^*_{initial} demonstrates the activity of the electrocatalyst throughout the stability test. The active sites were found to be stable and remained uniform within 200 concurrent cycles. Therefore, it is proposed that the catalysts were stable with no significant loss or degradation of their active sites.

The electrochemically active surface area (ECSA) of the $Ni(OH)_2$, I-doped $Ni(OH)_2$, and I_2-loaded $Ni(OH)_2$ electrocatalysts was also calculated in terms of the double-layer capacitance using a CV approach. As the ECSA is related to the electroactive sites of the electrocatalysts between the solid–liquid interphase, therefore, its measurements is critical to evaluate the catalyst performance. Fig. S4† represents the CV of bare CFC, pure $Ni(OH)_2$, I-doped $Ni(OH)_2$, and I_2-loaded $Ni(OH)_2$ electrocatalysts in the non-faradaic region, where the current was supposed to involve an electrical double-layer charging current. The graph between the scan rate *vs.* current density (Fig. 6) displayed a straight line and the slope of this linear graph was considered to be C_{dl}. The corresponding ECSA was calculated by dividing C_{dl} with the specific capacitance ($0.040\ cm^{-2}$).[45] A relatively higher ECSA was found in the case of I-doped $Ni(OH)_2$ than pristine $Ni(OH)_2$ and I_2-loaded $Ni(OH)_2$ electrocatalysts, as tabulated in Table 3. This high ECSA revealed the greater electrochemical surface area with greater exposed active sites, which in return was responsible for the superior electrocatalytic performance.

The electrochemical accessibility is another parameter to judge the performance of an electrocatalyst. For this, the integrated charge under the reduction peak of the cyclic voltammograms taken at a 20 mV s^{-1} scan rate was considered. Further, it was considered that a single oxygen atom was chemisorbed on one nickel atom. Therefore, the charge under the reduction peak was linked to the redox couple Ni^{2+}/Ni^{3+} and is given in Table 3. A higher value of the integrated area was found for I-doped $Ni(OH)_2$ electrocatalyst. Furthermore, the surface concentration of atoms was also calculated using the area under the reduction curve, again for I-doped $Ni(OH)_2$.[46] Conclusively, the measurements performed in the preliminary examinations suggested that the I-doped $Ni(OH)_2$ electrocatalyst had significant electrochemical stability, a high ECSA, and greater electroactive sites exposed to the surface of the prepared electrode. These results are key factors for enhancing the OER response of iodine-doped nickel hydroxide electrocatalysts.

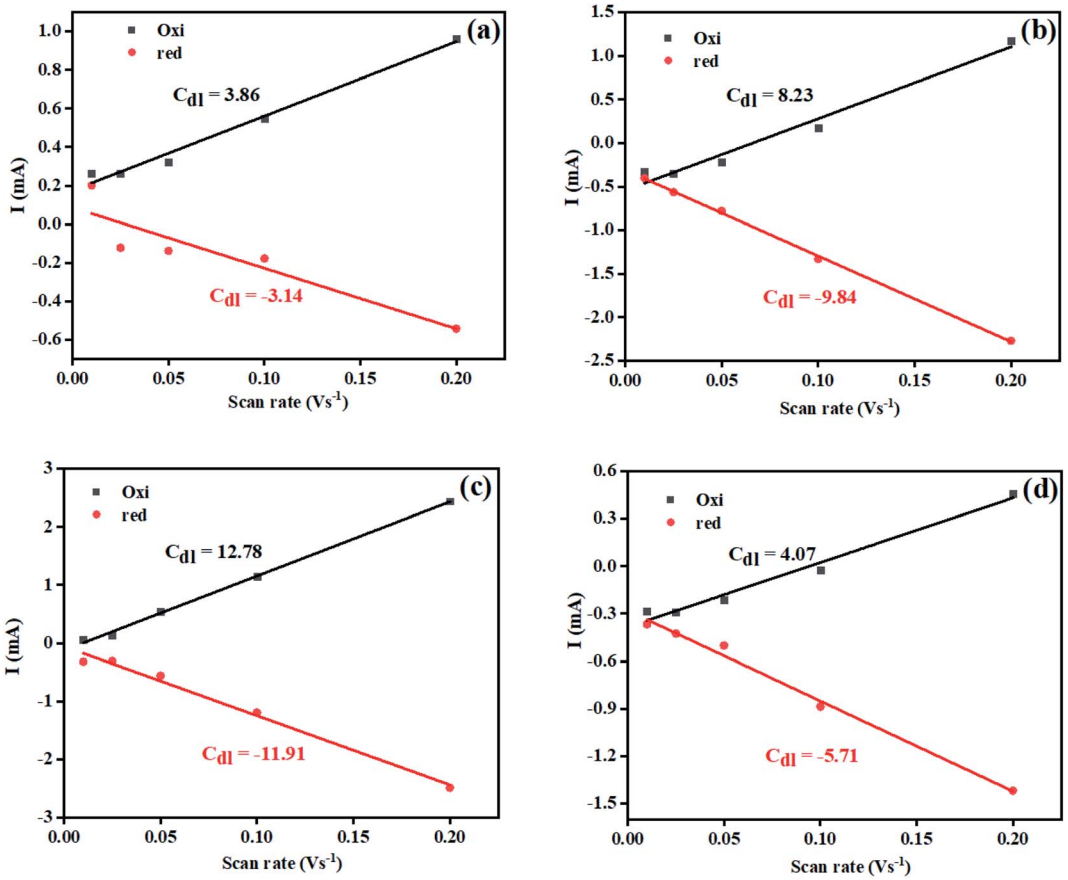

Fig. 6 Plot for calculation of the electrochemical active surface area for (a) bare CFC, (b) $Ni(OH)_2$, (c) I-doped $Ni(OH)_2$, and (d) I_2-loaded $Ni(OH)_2$ electrocatalysts.

Table 3 Different parameters calculated for evaluation of the OER performance of the pure $Ni(OH)_2$, I-doped $Ni(OH)_2$, and I_2-loaded $Ni(OH)_2$ electrocatalysts[a]

S. no.	Material	Average C_{dl} (cm^{-2})	ECSA (cm^2)	Onset potential (V *vs.* RHE)	Overpotential (V)			Tafel slope (mV dec^{-1})		R_{ct} (Ω)	Surface concentration of atoms ($\times 10^{16}$)	Exchange current density (mA cm^{-2})
					η_{40}	η_{100}	η_{350}	Lower OP	Higher OP			
1	$Ni(OH)_2$	9.04	226.04	1.53	440	680	—	66	268	8.8	2.52	0.7
2	I:$Ni(OH)_2$	12.34	308.72	1.52	330	390	630	46	104	2.3	15.94	2.79
3	I_2:$Ni(OH)_2$	4.89	122.35	1.62	720	—	—	60	275	4.0	4.27	1.60

[a] This suggests that I:$Ni(OH)_2$ had a greater OER efficiency than $Ni(OH)_2$.

Investigations into the electrical features and oxygen vacancies were done by the Mott–Schottky approach. This approach is considered an excellent tool to understand the electrical properties across the electrolyte–semiconductor interface.[47] Huang *et al.* analyzed the Mott–Schottky plots of WO and OVs rich WO_{3-x} and WO_3.[48] They noted a relative increase in the carrier density as a result of the OVs. Similarly, in order to confirm the OVs in iodine-doped $Ni(OH)_2$, Mott–Schottky analysis was also performed and the results are shown in Fig. S6.† The flat-band potential of $Ni(OH)_2$ was 0.03 and that of I-$Ni(OH)_2$ was −0.064 V. However, the Mott–Schottky plot of $Ni(OH)_2$ displayed a negative slope and behaved like a p-type material. Whereas, the Mott–Schottky plot of I-$Ni(OH)_2$ exhibited a positive slope and transformed to an n-type semiconductor material. This transformation of material from p-type to n-type was attributed to the iodine doping, which created OVs as a result of the iodine doping. Moreover, the charge-carrier density of iodine-doped nickel hydroxide was greater than that of pure nickel hydroxide, which again suggested the formation of OVs in the material. The Mott–Schottky results are tabulated in Table S1.† This improvement in carrier density in iodine-doped $Ni(OH)_2$ was attributed to the oxygen vacancies, which in turn acted as electron donors.[49]

2.3 OER activity

Owing to the exclusive structural and electrochemical redox competences, the electrochemical water oxidation-related performances of the pure $Ni(OH)_2$, I-doped $Ni(OH)_2$, and I_2-doped $Ni(OH)_2$ electrocatalysts were investigated using 1 M aqueous KOH solution. The anodic polarization measurements were performed by linear sweep voltammetry at a 5 mV s^{-1} scan rate with *iR* compensation, and the results are shown in Fig. 7(a). The Ni/$Ni(OH)_2$ oxidation peak appeared in the LSV of all the electrocatalysts. The oxidation peak started from 1.36 V to 1.48 V (*vs.* RHE). The onset potentials were found to be 1.53, 1.52, and 1.62 V (*vs.* RHE) for the $Ni(OH)_2$, I-doped $Ni(OH)_2$, and I_2-loaded $Ni(OH)_2$ electrocatalysts, respectively. After this potential regime, the current density increased sharply, which originated from the contribution of the catalytic current generated as a result of the water oxidation reaction. We were not able to report the overpotential at 10 mA cm^{-2} (η_{10}) current density due to the presence of an oxidation peak in that region. Therefore, the overpotentials for all the electrocatalysts were reported at 40 mA cm^{-2} (η_{40}). The values of the overpotential at the 40 mA cm^{-2} current density were 440, 330, and 720 mV for the pure $Ni(OH)_2$, I-doped $Ni(OH)_2$, and I_2-loaded $Ni(OH)_2$ electrocatalysts respectively. The increase in current density was very sharp in the case of I-doped $Ni(OH)_2$. At an overpotential of 390 mV, the current density was 100 mA cm^{-2} and at 630 mV, it was 350 mA cm^{-2}. However, at an overpotential of 630 mV, the $Ni(OH)_2$ electrocatalyst reached a current density of 144 mA cm^{-2}.

Additionally, the OER kinetics of the electrocatalysts was explored by constructing Tafel plots both in the lower and higher potential regions, as shown in Fig. 7(b).[50] At lower overpotential, the Tafel slopes for the $Ni(OH)_2$, I:$Ni(OH)_2$, and

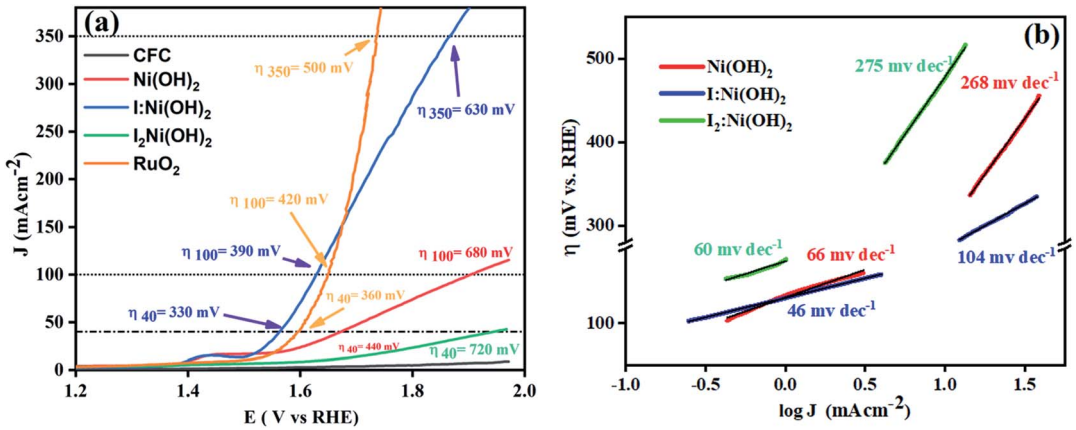

Fig. 7 OER electrocatalysis results: (a) LSV curve of the electrocatalysts taken at 5 mV s^{-1} and (b) corresponding Tafel plots in the low and high overpotential regions.

I_2:Ni(OH)$_2$ electrocatalysts were 66, 46, and 60 mV dec^{-1}, respectively. The Tafel slop of I:Ni(OH)$_2$ was lesser than that of the pure Ni(OH)$_2$ and I_2:Ni(OH)$_2$ electrocatalysts, which suggests the faster OER kinetics of the I:Ni(OH)$_2$ electrocatalyst. The Tafel slope for the I:Ni(OH)$_2$ electrocatalyst was nearly close to the value of 40 mV dec^{-1} that is characteristic for a single-electron electrochemical step as the rate-determining step.[51] However, at a higher overpotential, larger values of the Tafel slops were found, as given in Table 3, suggesting a greater polarization with the higher current density. Similarly, a lower Tafel slope suggests efficient electrocatalytic activity. At a higher overpotential, the I:Ni(OH)$_2$ electrocatalyst exhibited a Tafel slope of 104 mV dec^{-1}, which was nearly half that of the Ni(OH)$_2$ and I_2:Ni(OH)$_2$ electrocatalysts.

The changes in the Tafel slope from lower overpotential to higher overpotential were considered to be due to the change in the rate-determining step (RDS) or variations in the adsorption of intermediates resulting from the potential variations or the reduction in the electrode's effective surface area with the increasing gas evolution.[52] As the Tafel slope is inversely related with the charge-transfer coefficient, which is an experimental quantity, the greater the Tafel slope, the lower the charge-transfer coefficient and *vice versa*.[53] By considering the relation between the charge-transfer coefficient and Tafel slope, it was confirmed that I:Ni(OH)$_2$ exhibited better OER activity than the Ni(OH)$_2$ and I_2:Ni(OH)$_2$ electrocatalysts.

The stability of a catalyst is another important parameter for its potential applications. In this regard, multistep chronopotentiometry measurements without *iR* compensation were considered and the results are depicted in Fig. 8. The current density was increased from 4 to 48 mA cm^{-2} within 6 h of analysis. Among all 3 prepared electrocatalysts, I:Ni(OH)$_2$ exhibited the most stable current and potential, thus suggesting its long-term stability. An analogous trend was experienced during all the measured steps till it achieved a current density of 48 mA cm^{-2}.[46] These features demonstrated the steadiness of the material toward catalytic activity for OER catalysis and confirmed the relatively higher conductivity and superficial charge-transfer process on the exposed surface of the prepared electrode.[54] However, the multistep chronopotentiometry measurements of the nickel hydroxide and I_2-loaded nickel hydroxide electrocatalyst were not uniform throughout the

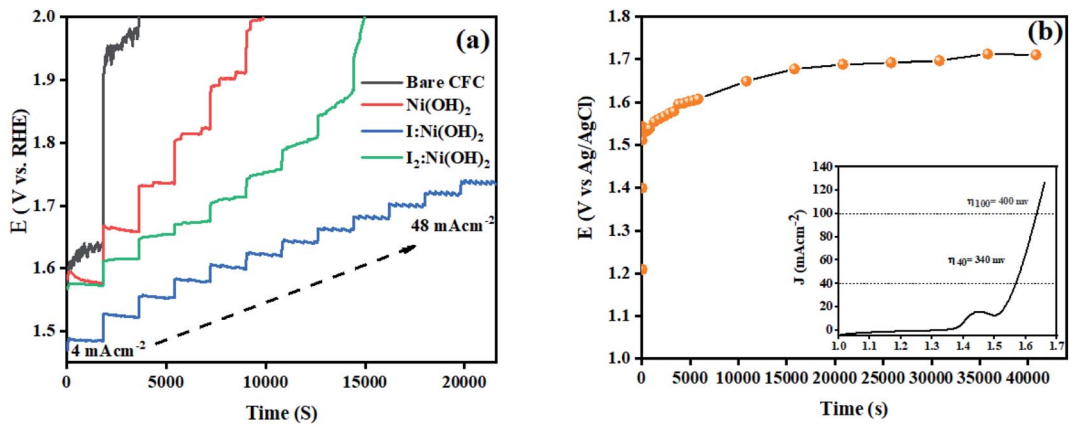

Fig. 8 Stability tests: (a) multistep chronopotentiometry from 4 to 48 mA cm^{-2} and (b) extended period chronopotentiometry (at 40 mA cm^{-2} current density) curve for the electrocatalysts using 1 M KOH electrolyte.

experiment and the materials failed to attain the required current density. This suggests that the $Ni(OH)_2$ and I_2-loaded $Ni(OH)_2$ electrocatalysts were not consistent during the catalytic process. Similarly, chronopotentiometry tests were also conducted at a 40 mA cm^{-2} current density for 12 h to check the materials' stability over an extended period of time. The results revealed little fluctuation in the overpotential with the passage of time. The inset of Fig. 8(b) shows the LSV curve of 1-$Ni(OH)_2$ after 12 h stability test. Similar to the extended period chronopotentiometry results, there was about a 10 mV increment in overpotential noticed.

Electrochemical impedance spectroscopy (EIS) was also considered to analyze the intrinsic OER kinetics of the $Ni(OH)_2$, I-doped $Ni(OH)_2$, and I_2-loaded $Ni(OH)_2$ electrocatalysts and the results are shown in Fig. 9. A modified Randles circuit was fitted to the experimental EIS data.† The inset of Fig. 9 shows the fitted circuit diagram. In this circuit, 'R_1' shows the solution resistance, 'R_{ct}' shows the charge-transfer resistance at the electrochemical double-layer, and 'R_f' is the resistance of a thin film of the material deposited on CFC.[55] The Nyquist plot of iodine-doped $Ni(OH)_2$ showed a smaller arc radius than the other materials tested. This was due to the faster kinetics of the electrode with efficient OER activity.[56] The calculated R_{ct} values for the bare CFC, $Ni(OH)_2$, I-doped $Ni(OH)_2$, and I_2-loaded $Ni(OH)_2$ electrocatalysts were 16.4, 8.8, 2.3, and 4.0 ohm, respectively. The lesser R_{ct} of the I-doped $Ni(OH)_2$ electrocatalysts suggested the faster electron-transfer process at their surfaces. This decrease in charge-transfer resistance was governed by the charge-trapping effect, reduction in flat-band protectional, and increase in charge-carrier density induced by iodine doping. This effect unblocked the transfer of charge at the I-$Ni(OH)_2$/electrolyte interfaces.[57,58]

The fundamental activity of the OER reaction and consequences of charge-transfer resistance were further analyzed in terms of the exchange current density (J°). The calculations of the exchange current density were done using $J^\circ = \frac{R \times T}{A \times n \times F \times \theta}$, where R = general gas constant, T = absolute temperature, A = geometric area of electrode, F = Faraday's constant, n = number of electrons, and θ = charge-transfer resistance.[59] The resultant exchange current densities for the CFC, $Ni(OH)_2$, I-doped $Ni(OH)_2$, and I_2-loaded $Ni(OH)_2$ electrocatalysts were 0.3, 0.7, 2.79, and 1.6 mA cm^{-2}, respectively. The higher value of exchange current density of the I-doped $Ni(OH)_2$ electrocatalyst showed its high intrinsic activity with quicker charge transfer across the electrode interphase.

The OER mechanism over the surface of hydroxides is considered to follow 4 crucial steps. The reaction mechanism is graphically illustrated in the graphical abstract and presented in eqn (1)–(4). The first step during this pathway involves the attachment of water molecules on active sites to give hydroxyl radicals. The prepared hydroxyl radicals dissociate to reactive

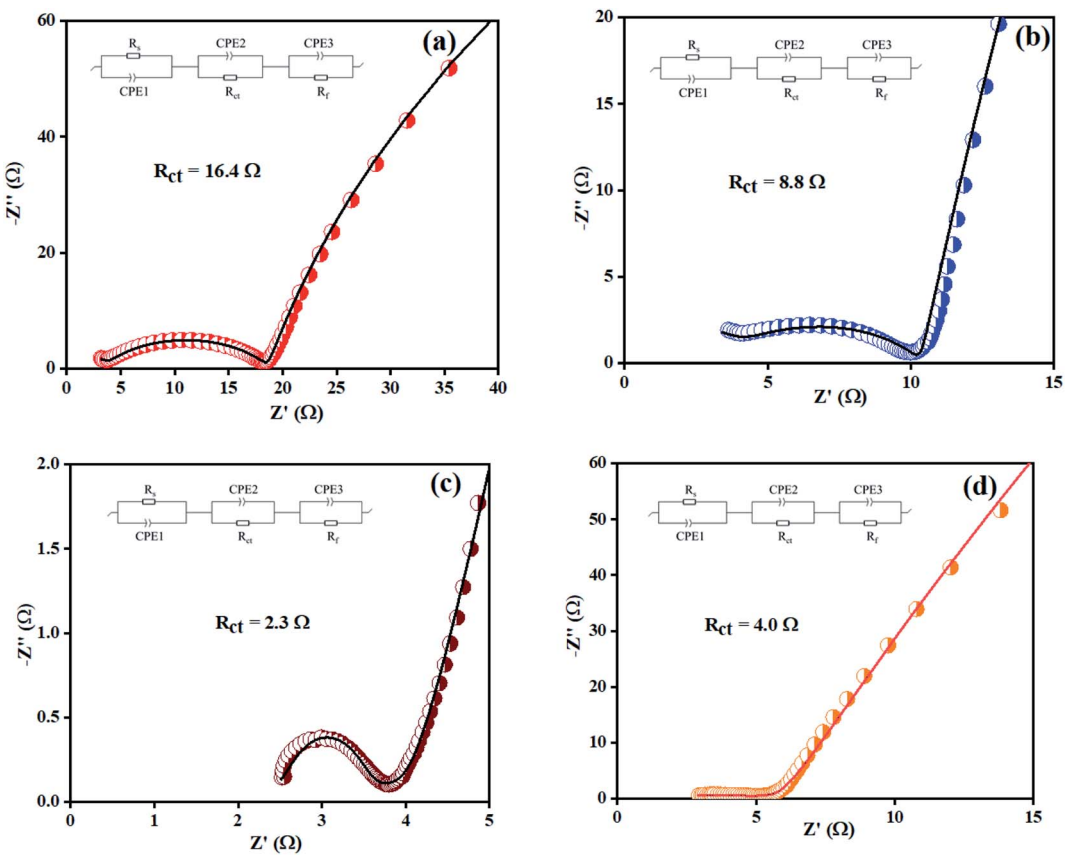

Fig. 9 EIS spectra of: (a) bare CFC, (b) $Ni(OH)_2$, (c) I-doped $Ni(OH)_2$, and (d) I_2-loaded $Ni(OH)_2$ electrocatalysts.

oxygen species. This generated reactive oxygen species react with water and are converted to peroxyl radicals. These peroxyl radicals leave the active sites followed by disintegration to oxygen molecules.[60]

$$H_2O + * \leftrightarrow OH* + H^+ + e^- \quad (1)$$

$$OH* \leftrightarrow O* + H^+ + e^- \quad (2)$$

$$H_2O + O* \leftrightarrow OOH* + H^+ + e^- \quad (3)$$

$$OOH* \leftrightarrow * + O_2 + H^+ + e^- \quad (4)$$

After the completion of the catalysis experiments, XRD, FESEM, and EDX analyses of the catalysts were conducted and the results are shown in Fig. 10. The XRD pattern of I-Ni(OH)$_2$ after the stability test showed all the characteristics peaks of the material but with additional broad bands, marked by *, which were confirmed to be for the carbon fiber cloth.[61] However, the peaks became broadened and their intensity dropped compared to the original ones. This drop in intensity might be due to the poisoning of the catalyst with the reaction intermediates, sample handling, and during its preparation for the XRD analysis. Moreover, the washing and drying of the samples also causes catalyst to loosen, which results in a decrease in the active parts of the catalyst. The FESEM analysis of the material after the stability test is also shown in Fig. 10(b). The FESEM results showed a little bit of aggregation of the material.[62] However, the material remained in its circular form. The EDX

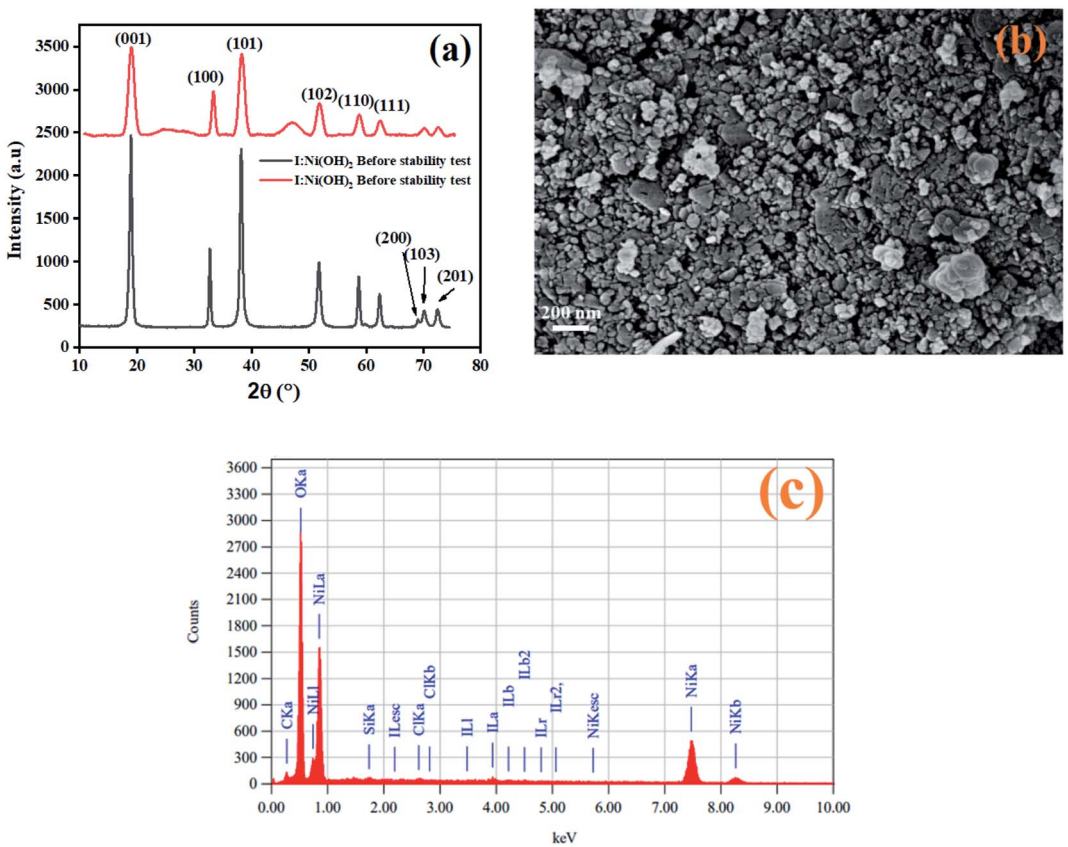

Fig. 10 Post characterization of I-Ni(OH)$_2$ by: (a) XRD, (b) FESEM, and (c) EDX.

Table 4 Benchmarking parameters for the previously reported electrocatalysts and comparison with the current study

Electrocatalysts	Electrolyte	Method of synthesis	Onset potential (V *vs.* RHE)	Overpotential (mV) η_{40}	Tafel slope (mV dec^{-1})	Ref.
I:Ni(OH)$_2$	1 M KOH	Hydrothermal	1.52	330	104	This work
β-Ni(OH)$_2$ NPs	1 M KOH	Precipitation	1.57	∼470	186	21
NiO-500	1 M KOH	Thermally oxidized	1.55	∼**370**	70	63
$NiCo_2O_4$	1 M NaOH	Solvothermal	1.53	∼310	53	64
$NiMnO_x$-B	6 M KOH	Annealing	1.60	∼400	69	65
NiMnLDH	6 M KOH	Annealing	1.63	∼440	83	65
NiO_x	0.1 M KOH	Thin-film deposition	1.52	390	65	66

analysis of the material after the stability test confirmed the presence of all the constituents in the material. The two extra elements found, carbon and silicon, might have originated from current collector (CFC) and washing process.

Consequently, the lower onset and overpotential, Tafel slope, multistep chronopotentiometric, EIS, and exchange current-density measurements suggest that the I-doped $Ni(OH)_2$ electrocatalyst exhibited better OER activity than the pure nickel hydroxide and I_2-loaded nickel hydroxide electrocatalysts. Owing to the following characteristics, the I-doped $Ni(OH)_2$ displayed a significantly improved alkaline OER process: (1) the nanostructured morphology with a greater pore diameter to size ratio, (2) the surface defects structure rich in oxygen vacancies, (3) the availability of more active sites and greater ECSA, (4) the lower charge-transfer resistance with a higher exchange current density, and (5) finally, the relatively lower Tafel slope. Moreover, the I_2-loaded $Ni(OH)_2$ electrocatalyst, due to its lower BET surface area, lower pore diameter to size ratio, and least stability, failed to perform similar to the I-doped $Ni(OH)_2$ electrocatalysts. Table 4 shows the benchmarking parameters for the previously reported electrocatalysts and a comparison with the current study.

3 Conclusion

In this report, we developed I-doped $Ni(OH)_2$ electrocatalysts through a hydrothermal method. Interestingly, the CFC-supported I-doped $Ni(OH)_2$ electrocatalyst exhibited greater electrocatalytic activity toward OER, requiring a lower overpotential of 330 mV to reach a current density of 40 mA cm^{-2} in 1 M aqueous KOH solution. Moreover, the I-doped $Ni(OH)_2$ electrocatalysts showed excellent longer term stability as tested from 4 to 48 mV cm^{-2}. The material exhibited a high electrochemical active surface area (308.72 cm^{-2}) and lower (2.3 ohm) charge-transfer resistance. The kinetic insights showed a lower Tafel slope of the materials as compared to their counterparts under identical conditions. The experienced superior electrocatalytic activity was considered to be due to the abundant oxygen vacancies, more exposed catalytic active sites at the surface, low charge-transfer resistance, and higher pore diameter to pore size ratio.

Conflicts of interest

There are no conflicts to declare.

Acknowledgements

Authors from the Islamia University of Bahawalpur highly acknowledge the Institute of Chemistry, BJ-Campus, The Islamia University of Bahawalpur-Pakistan and HEC-Islamabad (Pakistan). Dr Hamoud H. Somaily sincerely appreciates the King Khalid University for the research grant (KKU/RCAMS/22) under the Research Center for Advanced Materials Science (RCAMS) at King Khalid University, Saudi Arabia. Prof. Dr Sonia Zulfiqar is highly thankful to the American University in Cairo for financial support through STRC mini-grant and research project no. SSE-CHEM-S. Z.- FY19-FY20-FY21-RG(1-19)-2018-Oct-01-17-53-22.

References

1 R. S. Gohar, I. Ahmad, A. Shah, S. Majeed, M. Najam-ul-Haq and M. N. Ashiq, *Journal of Energy Storage*, 2020, **31**, 101621.
2 P. Moriarty and D. Honnery, in *Clean Energy for Sustainable Development*, ed. M. G. Rasul, A. k. Azad and S. C. Sharma, Academic Press, 2017, pp. 3–27.
3 I. Ahmad, J. Ahmed, S. Batool, M. N. Zafar, A. Hanif, Zahidullah, M. F. Nazar, A. Ul-Hamid, U. Jabeen, A. Dahshan, M. Idrees and S. A. Shehzadi, *J. Alloys Compd.*, 2022, **894**, 162409.
4 R. G. Jadhav, D. Singh, P. V. Krivoshapkin and A. K. Das, *Inorg. Chem.*, 2020, **59**, 7469–7478.
5 J. Liu, J. Wang, B. Zhang, Y. Ruan, H. Wan, X. Ji, K. Xu, D. Zha, L. Miao and J. Jiang, *J. Mater. Chem. A*, 2018, **6**(5), 2067–2072.
6 N. A. Khan, N. Rashid, M. Junaid, M. N. Zafar, M. Faheem and I. Ahmad, *ACS Appl. Energy Mater.*, 2019, **2**(5), 3587–3594.
7 C. Wu, Y. Du, Y. Fu, W. Wang, T. Zhan, Y. Liu, Y. Yang and L. Wang, *Composites, Part B*, 2019, **177**, 107252.
8 J. Guan, X. Bai and T. Tang, *Nano Res.*, 2022, **15**, 818–837.
9 Z. Gao, L. L. Gong, X. Q. He, X. M. Su, L. H. Xiao and F. Luo, *Inorg. Chem.*, 2020, **59**, 4995–5003.
10 Y. Lee, J. Suntivich, K. J. May, E. E. Perry and Y. Shao-Horn, *J. Phys. Chem. Lett.*, 2012, **3**, 399–404.
11 F. Song, L. Bai, A. Moysiadou, S. Lee, C. Hu, L. Liardet and X. Hu, *J. Am. Chem. Soc.*, 2018, **140**, 7748–7759.
12 S. Kumaravel, K. Karthick, S. S. Sankar, A. Karmakar, R. Madhu, K. Bera and S. Kundu, *Sustainable Energy Fuels*, 2021, **5**, 6215–6268.
13 D. Zhou, P. Li, X. Lin, A. McKinley, Y. Kuang, W. Liu, W.-F. Lin, X. Sun and X. Duan, *Chem. Soc. Rev.*, 2021, **50**, 8790–8817.
14 C. Hu, Q. Dai and L. Dai, *Cell Rep. Phys. Sci.*, 2021, **2**, 100328.
15 M. Gao, W. Sheng, Z. Zhuang, Q. Fang, S. Gu, J. Jiang and Y. Yan, *J. Am. Chem. Soc.*, 2014, **136**, 7077–7084.
16 M.-R. Gao, X. Cao, Q. Gao, Y.-F. Xu, Y.-R. Zheng, J. Jiang and S.-H. Yu, *ACS Nano*, 2014, **8**, 3970–3978.
17 V. Vij, S. Sultan, A. M. Harzandi, A. Meena, J. N. Tiwari, W.-G. Lee, T. Yoon and K. S. Kim, *ACS Catal.*, 2017, **7**, 7196–7225.
18 M. S. Ali Akbari, R. Bagheri, Z. Song and M. M. Najafpour, *Sci. Rep.*, 2020, **10**, 8757.
19 Y. R. Hong, K. Kim, J. H. Ryu, S. Mhin, J. Kim, G. Ali, K. Y. Chung, S. Kang and H. Han, *Adv. Funct. Mater.*, 2020, **30**, 2004330.
20 D. Xiong, W. Li and L. Liu, *Chem.–Asian J.*, 2017, **12**, 543–551.
21 N. Kim, D. Lim, Y. Choi, S. E. Shim and S.-H. Baeck, *Electrochim. Acta*, 2019, **324**, 134868.
22 D. S. Hall, D. J. Lockwood, S. Poirier, C. Bock and B. R. MacDougall, *J. Phys. Chem. A*, 2012, **116**, 6771–6784.
23 T. N. Ramesh, *Mater. Chem. Phys.*, 2009, **114**, 618–623.

24 D. Hall, D. Lockwood, C. Bock and B. MacDougall, *Proc. R. Soc. A*, 2015, **471**, 1–65.
25 A. Vazhayil, L. Vazhayal, J. Thomas, S. Ashok and N. Thomas, *Appl. Surf. Sci.*, 2021, **6**, 100184.
26 Z. Angeles-Olvera, A. Crespo-Yapur, O. Rodríguez, J. L. Cholula-Díaz, L. M. Martínez and M. Videa, *Energies*, 2022, **15**, 1609.
27 K. P. Madhuri, N. S. John, S. Angappane, P. K. Santra and F. Bertram, *J. Phys. Chem. C*, 2018, **122**, 28075–28084.
28 L.-F. Chen, Z.-Y. Yu, J.-J. Wang, Q.-X. Li, Z.-Q. Tan, Y.-W. Zhu and S.-H. Yu, *Nano Energy*, 2015, **11**, 119–128.
29 N. Hussain, W. Yang, J. Dou, Y. Chen, Y. Qian and L. Xu, *J. Mater. Chem. A*, 2019, **7**, 9656–9664.
30 K. P. Madhuri, P. Kaur, M. E. Ali and N. S. John, *J. Phys. Chem. C*, 2017, **121**, 9249–9259.
31 W. Li, R. Liang, A. Hu, Z. Huang and Y. N. Zhou, *RSC Adv.*, 2014, **4**, 36959–36966.
32 J. Zhang, Z.-H. Huang, Y. Xu and F. Kang, *Int. J. Photoenergy*, 2012, **2012**, 915386.
33 M. Szkoda, K. Siuzdak and A. Lisowska-Oleksiak, *Phys. E*, 2016, **84**, 141–145.
34 Y.-Z. Zheng, X. Tao, Q. Hou, D.-T. Wang, W.-L. Zhou and J.-F. Chen, *Chem. Mater.*, 2011, **23**, 3–5.
35 H. Lee, X. Zhang, B. Kim, J.-H. Bae and J. Park, *Materials*, 2021, **14**, 6118.
36 V. Štengl and T. M. Grygar, *Int. J. Photoenergy*, 2011, **2011**, 685935.
37 W. Su, Y. Zhang, Z. Li, L. Wu, X. Wang, J. Li and X. Fu, *Langmuir*, 2008, **24**, 3422–3428.
38 Z. He, C. Wang, H. Wang, F. Hong, X. Xu, J. Chen and S. Song, *J. Hazard. Mater.*, 2011, **189**, 595–602.
39 A. Umar, V. Mohammad and Y.-B. Hahn, *Metal Oxide Nanostructures and Their Applications*, American Scientific Publishers, 2010, ch. 2, pp. 1–39.
40 S. Vidhya, *Nickel–cobalt hydroxide: a positive electrode for supercapacitor applications*, 2020.
41 C. Krishnan, P. Selvarajan, T. H. Freeda and C. K. Mahadevan, *Phys. B*, 2009, **404**, 289–294.
42 T. Audichon, T. W. Napporn, C. Canaff, C. Morais, C. Comminges and K. B. Kokoh, *J. Phys. Chem. C*, 2016, **120**, 2562–2573.
43 K. S. Joya, M. A. Ehsan, N.-U.-A. Babar, M. Sohail and Z. H. Yamani, *J. Mater. Chem. A*, 2019, **7**, 9137–9144.
44 K. Joya, N. Babar, S. Gilani, F. Yasmeen, M. Sarfaraz, S. Ikram, S. Colak, K. Ocakoglu and M. Ince, *ChemistrySelect*, 2018, **3**, 11357–11366.
45 C. C. L. McCrory, S. Jung, J. C. Peters and T. F. Jaramillo, *J. Am. Chem. Soc.*, 2013, **135**, 16977–16987.
46 N.-U.-A. Babar and K. S. Joya, *ACS Omega*, 2020, **5**, 10641–10650.
47 Y. Yang, H. Wang, L. Wang, Y. Ge, K. Kan, K. Shi and J. Chen, *New J. Chem.*, 2016, **40**, 4678–4686.
48 Z.-H. Huang, H. Li, W.-H. Li, G. Henkelman, B. Jia and T. Ma, *Small*, 2020, **16**, 2004709.
49 L. Mentar, H. Lahmar, K. mohamed redha and A. Amor, *J. New Technol. Mater.*, 2014, **4**, 41–45.
50 S. Anantharaj, S. Noda, M. Driess and P. W. Menezes, *ACS Energy Lett.*, 2021, **6**, 1607–1611.
51 Z. Lu, W. Xu, W. Zhu, Q. Yang, X. Lei, J. Liu, Y. Li, X. Sun and X. Duan, *Chem. Commun.*, 2014, **50**, 6479–6482.
52 T. Shinagawa, A. T. Garcia-Esparza and K. Takanabe, *Sci. Rep.*, 2015, **5**, 13801.
53 L. Negahdar, F. Zeng, S. Palkovits, C. Broicher and R. Palkovits, *ChemElectroChem*, 2019, **6**, 5588–5595.
54 M. A. Ghanem, M. S. Amer, A. M. Al-Mayouf, P. Arunachalam and M. T. Weller, *Catalysts*, 2021, **11**, 1408.
55 K. Feng, F. Wang, X. Yang, H. Zhang, X. Li and H. Zhang, *J. Mater. Chem. A*, 2019, **7**, 567–573.
56 K.-B. Pu, C.-X. Lu, K. Zhang, H. Zhang, Q.-Y. Chen and Y.-H. Wang, *Bioprocess Biosyst. Eng.*, 2020, **43**, 429–437.
57 J. X. Zhao, Y. Z. Zheng, X. H. Lu, J. F. Chen, X. Tao and W. Zhou, *ChemPhysChem*, 2013, **14**, 1977–1984.
58 W.-H. Yang, W.-T. Yang and X.-Y. Lin, *Acta Phys.-Chim. Sin.*, 2012, **28**, 831–836.
59 S. Anantharaj, S. R. Ede, K. Sakthikumar, K. Karthick, S. Mishra and S. Kundu, *ACS Catal.*, 2016, **6**, 8069–8097.
60 X. Bai, Z. Duan, B. Nan, L. Wang, T. Tang and J. Guan, *Chin. J. Catal.*, 2022, **43**, 2240–2248.
61 T. Yu, H. L. Liu, M. Huang, J. Zhang, D. Su, Z. Tang, J. Xie, Y. Liu, A. Yuan and Q. Kong, *RSC Adv.*, 2017, **7**, 51807–51813.
62 J. Li, P. Li, J. Li, Z. Tian and F. Yu, *Catalysts*, 2019, **9**, 506.
63 P. T. Babar, A. C. Lokhande, M. G. Gang, B. S. Pawar, S. M. Pawar and J. H. Kim, *J. Ind. Eng. Chem.*, 2018, **60**, 493–497.
64 X. Gao, H. Zhang, Q. Li, X. Yu, Z. Hong, X. Zhang, C. Liang and Z. Lin, *Angew. Chem.*, 2016, **55**, 6290–6294.
65 Z. Chen, Z. Wang, R. Cai, Y. Xie, J. Yu, X. Long, B. Yang and S. Yang, *Nanoscale*, 2020, **12**, 2472–2478.
66 H. Radinger, P. Connor, S. Tengeler, R. W. Stark, W. Jaegermann and B. Kaiser, *Chem. Mater.*, 2021, **33**, 8259–8266.